Modelling the longitudinal failure of fibre-reinforced composites at microscale

Catalanotti, G.; Varandas, L. F.; Melro, António R.; Sebaey, T. A.; Bessa, M. A.; Falzon, B. G.

DOI
10.1016/B978-0-12-818984-9.00012-3

Publication date
2020

Document Version
Final published version

Published in
Multi-Scale Continuum Mechanics Modelling of Fibre-Reinforced Polymer Composites

Modelling the longitudinal failure of fiber-reinforced composites at microscale

12

G. Catalanotti[1], L.F. Varandas[1], António R. Melro[2], T.A. Sebaey[3], M.A. Bessa[4] and B.G. Falzon[1]

[1]Advanced Composites Research Group, School of Mechanical and Aerospace Engineering, Queen's University Belfast, Belfast, United Kingdom, [2]Bristol Composites Institute (ACCIS), University of Bristol, Bristol, United Kingdom, [3]Engineering Management Department, College of Engineering, Prince Sultan University, Riyadh, Saudi Arabia, [4]Faculty of Mechanical, Maritime and Materials Engineering, Delft University of Technology, Delft, the Netherlands

Chapter points

- An algorithm is proposed for the generation of representative volume elements (RVEs) with misaligned fibers. The fibers are modelled as Bézier curves whose control points are moved in a semistochastic fashion in order to introduce waviness. The algorithm consists of two components: a stochastic process and an optimization procedure. The latter ensures that the waviness of the RVEs is statistically representative of the actual material.
- A computational framework to model the longitudinal failure of fiber-reinforced composites, in both tension and compression is presented. An analysis of the material failure onset and propagation is conducted with respect to the misalignment angle distribution in order to understand its effect.

12.1 Introduction

Micromechanical analysis can be classified as a powerful means to increase the understanding of the effect of material architecture and properties of the constituents on the overall mechanical response of unidirectional (UD) composites. Its use can serve many purposes: (1) gain unique insights on the damage onset and propagation in the material; (2) allow the application of complex stress states otherwise difficult to enforce experimentally; and (3) generate failure envelopes, providing a way to validate analytical failure criteria (Camanho et al., 2015).

The focus of this chapter resides in the longitudinal failure of UD composites, in both tension and compression. The difficulty in modelling such failure types lies in the fact that complex damage mechanisms arise and their modelling requires special care.

Multi-Scale Continuum Mechanics Modelling of Fibre-Reinforced Polymer Composites.
DOI: https://doi.org/10.1016/B978-0-12-818984-9.00012-3

Longitudinal failure in tension is characterized by a complicated process involving the preliminary fracture of individual fibers, the formation of clusters of fractured fibers, and ultimately, the final failure of the composite. Modelling this type of damage mechanism requires the use of extremely large RVEs, which the associated computational cost is often prohibitive. Differently, longitudinal failure in compression is associated with the onset and propagation of a kink-band, a complex failure mechanism that consists of different steps: the initial rotation of the fibers; followed by shear failure of the matrix, causing an unstable condition with the formation of a kink-band; the progressive bending/shearing deformation, causing softening of the material; and finally, the steady-state band broadening terminated by fiber snapping. Again, modelling this complex failure mechanism requires the use of large RVEs and similar considerations apply with regard to their computational cost.

Fibrous reinforcements, which are embedded in the matrix material, possess a certain waviness (or misalignment). Modelling-wise, their misalignment is often neglected, due to its difficulty. This may be justifiable when modelling the transverse failure of the material. However, it should be considered when modelling the longitudinal failure of the composite. Several approaches have been proposed to model *regular* or *stochastic* waviness, but none of them is able to ensure that the modelled misalignment is statistically representative of the actual waviness of the material, except for the approach proposed in the following, where the statistical representativeness of the fiber misalignment is addressed.

In the following, all points mentioned above will be discussed and reviewed in detail at the beginning of each section. The structure of this chapter is organized as follows: Section 12.2 presents a methodology for the modelling of fiber waviness; in Section 12.3, the main constitutive models for the material constituents and the interface are reported; and finally, in Section 12.4, micromechanical analyses are reported and discussed for longitudinal loading, in both tension and compression.

12.2 Representative volume element generation: focusing on the fiber waviness

High-fidelity micromechanical analyses of fiber-reinforced composites rely on the detailed description of the material microstructure. To this end, several have been the algorithms proposed for the generation of RVEs, and of which a summary is reported in Chapter 2, Microscale Representative Volume Element—Generation and Statistical Characterization, of this book. This effort has consisted of modelling UD fiber-reinforced polymers (FRPs) by means of two-dimensional (2D) RVEs, where the target has been on the generation ofthe 2D fiber distribution (Melro et al., 2008; Vaughan and McCarthy, 2011). Three-dimensional (3D) RVEs have been obtained by extruding the 2D RVEs in the longitudinal (fiber) direction, consequently considering all fibers to be perfectly aligned and parallel.

In reality, fibers are not all perfectly aligned, and their misalignment needs to be taken into account. This waviness has been modelled as *regular*, when an analytical

expression is assumed, or *random*, which is generated through a stochastic process. Neglecting the first case, since it is too simplistic for a high-fidelity simulation, the algorithms able to model waviness in fibrous materials (Faessel et al. (2005), Altendorf and Jeulin (2011), Herasati and Zhang (2014), Recchia et al. (2014), and Stein et al. (2015) have failed in ensuring the numerical misalignment to be statistically representative of the experimental one.

To the authors' knowledge, the methodology recently proposed by Sebaey et al. (2019) and by Catalanotti and Sebaey (2019) is the only one being able to generate a statistically representative numerical fiber distribution. Its details are given in the following.

12.2.1 Spatial descriptors for fiber waviness

Let x, y, and z be the longitudinal, transverse, and through-thickness directions of the material, and $\hat{\boldsymbol{i}}$, $\hat{\boldsymbol{j}}$, and $\hat{\boldsymbol{k}}$ the associated relative unit vectors, respectively. Despite the different approaches proposed (Yurgartis, 1987; Clarke et al., 1995; Creighton et al., 2001; Kratmann et al., 2009; Requena et al., 2009; Sutcliffe et al., 2012), it is convenient to take the following spatial descriptors (Fig. 12.1):

- ϕ_{zx}, the angle that the projection of the tangent vector $\boldsymbol{v}$ onto the plane of normal $\hat{\boldsymbol{k}}$ (plane in green in Fig. 12.1),

$$\text{proj}_{\hat{\boldsymbol{k}}}(\boldsymbol{v}) = \boldsymbol{v} - \left(\boldsymbol{v} \cdot \hat{\boldsymbol{k}}\right)\hat{\boldsymbol{k}} \tag{12.1}$$

  forms with the nominal direction of the fiber, $\hat{\boldsymbol{i}}$,

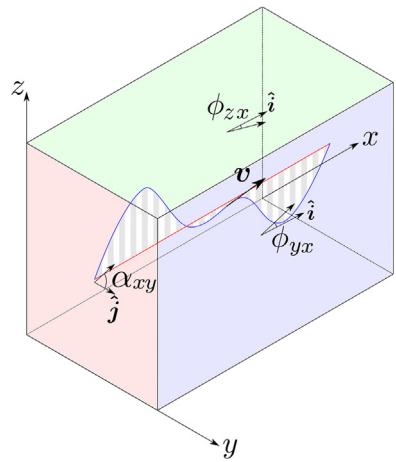

Figure 12.1 Angles that characterize fiber misalignment.
Source: After Catalanotti, G., Sebaey, T., 2019. An algorithm for the generation of three-dimensional statistically representative volume elements of unidirectional fiber-reinforced plastics: focusing on the fibres waviness. Compos. Struct. 227, 111272.

$$\phi_{zx} = \frac{\text{arccosproj}\hat{\boldsymbol{k}}(\boldsymbol{v}) \cdot \hat{\boldsymbol{i}}}{\left\|\text{proj}\hat{\boldsymbol{k}}(\boldsymbol{v})\right\|} \tag{12.2}$$

- ϕ_{yx}, the angle that the projection of the tangent vector $\boldsymbol{v}$ onto the plane of normal $\hat{\boldsymbol{j}}$ (plane in blue in Fig. 12.1),

$$\text{proj}\hat{\boldsymbol{j}}(\boldsymbol{v}) = \boldsymbol{v} - \left(\boldsymbol{v} \cdot \hat{\boldsymbol{j}}\right)\hat{\boldsymbol{j}} \tag{12.3}$$

forms with the nominal direction of the fiber, $\hat{\boldsymbol{i}}$,

$$\phi_{zx} = \frac{\text{arccosproj}\hat{\boldsymbol{j}}(\boldsymbol{v}) \cdot \hat{\boldsymbol{i}}}{\left\|\text{proj}\hat{\boldsymbol{j}}(\boldsymbol{v})\right\|} \tag{12.4}$$

- α_{xy}, the angle that the projection of the tangent vector $\boldsymbol{v}$ onto the plane of normal $\hat{\boldsymbol{i}}$ (plane in red in Fig. 12.1),

$$\text{proj}\hat{\boldsymbol{i}}(\boldsymbol{v}) = \boldsymbol{v} - \left(\boldsymbol{v} \cdot \hat{\boldsymbol{i}}\right)\hat{\boldsymbol{i}} \tag{12.5}$$

forms with the transverse direction, $\hat{\boldsymbol{j}}$,

$$\alpha_{xy} = \frac{\text{arccosproj}\hat{\boldsymbol{i}}(\boldsymbol{v}) \cdot \hat{\boldsymbol{j}}}{\left\|\text{proj}\hat{\boldsymbol{i}}(\boldsymbol{v})\right\|} \tag{12.6}$$

Of these three angles, α_{xy} has no importance since it does not affect the homogenized material properties in compression. Moreover, measuring α_{xy} is not an easy task.

On the contrary, the in-plane and out-of-plane misalignment angles, ϕ_{zx} and ϕ_{yx}, respectively, are known to have an influence on the longitudinal compressive response. In composites, these two angles may assume to be different or the same, depending on the manufacturing process. In the following, we will indicate any of the two angles as ϕ in order to simplify the notation.

12.2.2 Algorithm for representative volume element generation

12.2.2.1 Modelling the waviness of the fibers

The fibers are modelled as Bézier curves, and misalignment is introduced moving their control points following a stochastic process. Initially, the position of the perfectly aligned fibers is calculated following the procedure proposed by Catalanotti (2016); when the desired distribution is achieved, misalignment is introduced.

Considering the coordinate system previously presented (Fig. 12.1), let the RVE be prismatic and with dimensions $H_x \times H_y \times H_z$, let n_F be the number of fibers and n the number of control points of each Bézier curve (from 0 to $n-1$). Each fiber can be expressed as:

$$\mathbf{B}(t) = \sum_{i=0}^{n} \binom{n}{i} (1-t)^{n-i} t^i \mathbf{P}_i, \qquad 0 \le t \le 1 \tag{12.7}$$

where $\boldsymbol{P}_i = \{x_i, y_i, z_i\}^T$ are the coordinates of the ith control point. Therefore, in the RVE, there will be $n \cdot n_F$ control points, from 0 to $n_F \cdot n - 1$, and these can be moved in order to achieve the desired misalignment. This is done in several iterations. At the Ith iteration, the randomized sequence of integers from 0 to $n_F \cdot n - 1$, π_I, is calculated. Iterating over this sequence, the Jth element will isolate a control point, $K = \pi_I(J)$, which is selected and moved. Its position that was calculated in the iteration $I - 1$ will be updated as following:

$$\boldsymbol{P}_K^I = \boldsymbol{P}_K^{I-1} + \boldsymbol{u}_K^I \tag{12.8}$$

assuming the displacement $\boldsymbol{u}_K^I$ to be:

$$\boldsymbol{u}_K^I = \rho_K^I \{0, \cos\theta_K^I, \sin\theta_K^I\}^T \tag{12.9}$$

where θ_K^I and ρ_K^I are the coordinates of the control point with respect to the polar coordinate system lying on the plane perpendicular to x and with origin at $\boldsymbol{P}_K^{I-1}$ (Fig. 12.2).

The angular coordinate, θ_K^I, is chosen to be:

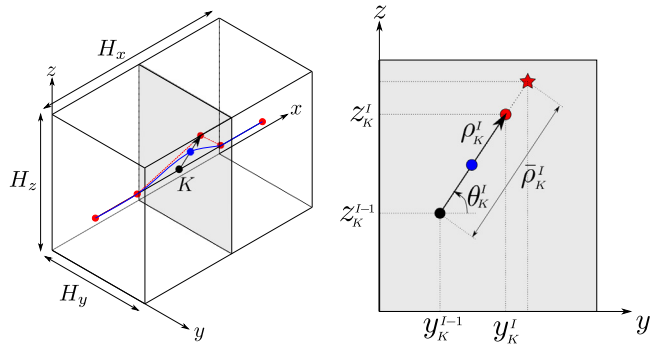

(A) (B)

Figure 12.2 Schematic representation of a fiber as a Bézier curve and relative control polygon: (A) 3D view and (B) planar view. The black and red circles indicate the position of the control point at iteration $I - 1$ and I, respectively. The blue circle is the center of the intersection between the fiber and the plane of normal $\hat{\boldsymbol{i}}$. The star indicates the furthest position that could be assumed by the control point K at iteration I.
Source: After Catalanotti, G., Sebaey, T., 2019. An algorithm for the generation of three-dimensional statistically representative volume elements of unidirectional fiber-reinforced plastics: focusing on the fibres waviness. Compos. Struct. 227, 111272.

$$\theta_K^I = 2\pi\mathscr{U} \tag{12.10}$$

where $\mathscr{U}$ is a continuous random variable uniformly distributed in the interval $[0, 1]$.

The radial coordinate ρ_K^I is selected through a stochastic process, in the range $\left[0,\overline{\rho}_K^I\right]$, where $\overline{\rho}_K^I$ is the maximum value that can be assumed by ρ_K^I before occurring interpenetration between the fiber owning the control point K and the surrounding ones.

12.2.2.2 Determination of the radial coordinate ρ_K^I

By applying the aforementioned stochastic process, the misalignment can be introduced in the fibers (Fig. 12.3), and the distribution of the misalignment angle, ϕ, can be calculated estimating the tangent at several points of the Bézier curves. This distribution, however, will still not be statistically representative of the misalignment angle distribution determined experimentally.

In order to ensure the statistical representativeness of the numerical distribution, Catalanotti and Sebaey (2019) proposed to combine the stochastic process with an optimization procedure. The numerical distribution was obtained by choosing the value of ρ_K^I which minimizes the difference between the numerical and experimental distributions. This is achieved by considering the likelihood and the probability of the two distributions.

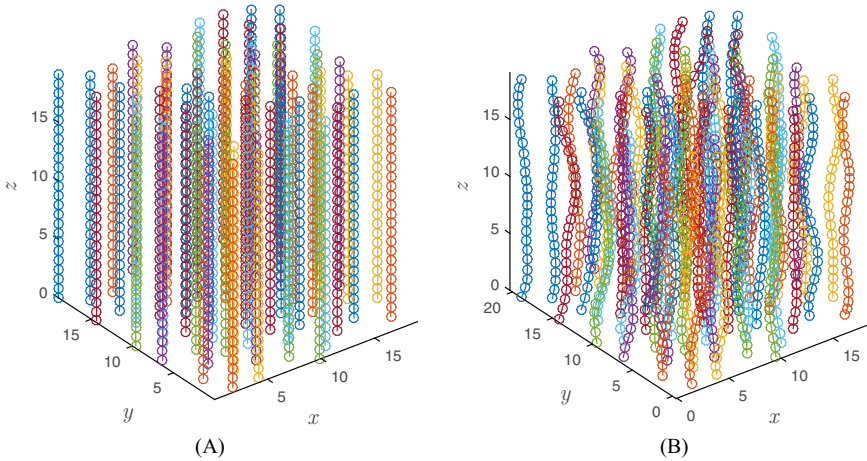

Figure 12.3 Fiber misalignment through the perturbation process: (A) initial configuration and (B) perturbed configuration.
Source: After Catalanotti, G., Sebaey, T., 2019. An algorithm for the generation of three-dimensional statistically representative volume elements of unidirectional fiber-reinforced plastics: focusing on the fibres waviness. Compos. Struct. 227, 111272.

Minimizing the standard error of the likelihood

If the likelihood is considered, λ_I^K is selected in order to minimize the standard error (SE) of the maximum likelihood estimate (MLE). If $\hat{\phi}$ is the MLE parameter for ϕ, the SE reads:

$$\mathrm{SE}\left(\hat{\phi}\right) = \sqrt{\mathrm{Var}\left(\hat{\phi}\right)} \tag{12.11}$$

where $\mathrm{Var}\left(\hat{\phi}\right)$ is the asymptotic covariance matrix which, at the Ith iteration, takes the value of $\mathrm{SE}\left(\hat{\phi}\left(\lambda_I^K\right)\right)$. Therefore, λ_I^K can be selected in order to minimize the SE. If, for example, the misalignment angle distributes as a von Mises distribution of mean direction μ, and concentration parameter κ, its probability density function is given by Mardia and Jupp (2008):

$$g(\phi;\mu,\kappa) = \frac{1}{2\pi I_0(\kappa)} \mathrm{e}^{\kappa cos(\phi-\mu)} \tag{12.12}$$

where I_0 is the modified Bessel function of the first kind and order 0. In this case, if $\left(\phi_1,\ldots,\phi_j,\ldots,\phi_N\right)$ is a random sample from the same distribution, the MLE for the mean direction is simply $\hat{\mu} = \overline{\phi}$, where $\overline{\phi}$ is the circular mean of ϕ_j, while the MLE for the concentration parameter, $\hat{\kappa}$, is obtained solving the equation $A(\hat{\kappa}) = \overline{R}$, where:

$$A(\kappa) = I_1(\kappa)/I_0(\kappa) \tag{12.13}$$

and the *mean resultant length*, $\overline{R}$, reads:

$$\overline{R} = \sqrt{\overline{C}^2 + \overline{S}^2}; \quad \overline{C} = \frac{1}{N}\sum_{j=1}^{N} \cos\phi_j; \quad \overline{S} = \frac{1}{N}\sum_{j=1}^{N} \sin\phi_j \tag{12.14}$$

Since the mean direction has to be the longitudinal direction of the composite, it can be imposed that $\mu = 0$, making the angular distribution to be fully characterized by the MLE parameter, $\hat{\kappa}$. Minimizing the SE at each iteration yields the desired numerical distribution (Fig. 12.4).

The experimental distributions are determined through the usage of computed tomography (CT) scans, allowing for the footprint of individual fibers to be tracked and fit the obtained data using the von Mises distribution presented in Eq. (12.12), thus quantifying the experimental degree of fiber misalignment (Sebaey et al., 2019).

Minimizing the standard error of the probability

If $Q(p)$ denotes the quantile function, and $\boldsymbol{Y}$ and $\hat{\boldsymbol{Y}}$ are the vectors containing the p-quantiles calculated at the values $\{1/p, 2/p, \ldots, (p-1)/p\}$ for the experimental

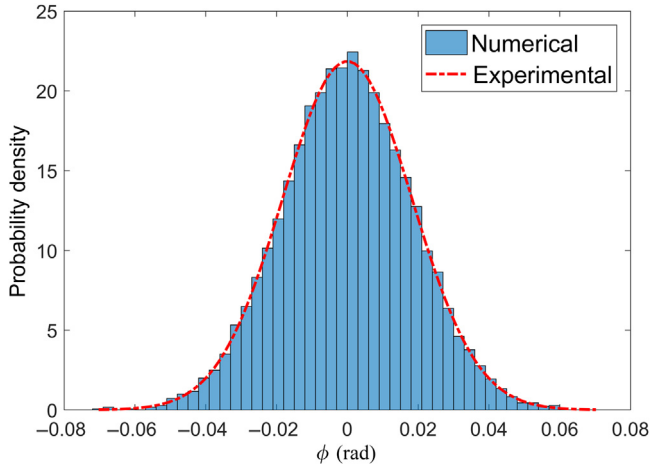

Figure 12.4 Experimental and numerical distributions obtained by minimizing the SE of the likelihood.
Source: After Catalanotti, G., Sebaey, T., 2019. An algorithm for the generation of three-dimensional statistically representative volume elements of unidirectional fiber-reinforced plastics: focusing on the fibres waviness. Compos. Struct. 227, 111272.

and numerical distributions, respectively, the two distributions can be matched minimizing the SE defined as:

$$\mathrm{SE} = \sqrt{\frac{1}{p}\sum_{i}^{p}\left[\boldsymbol{Y}(p) - \hat{\boldsymbol{Y}}\left(p\left(\lambda_I^K\right)\right)\right]} \tag{12.15}$$

The match between the two distributions is noteworthy (Fig. 12.5B). It should be observed that, in this case, it is not necessary to assume any analytical formulation for the misalignment angle.

12.2.2.3 Periodicity of the representative volume element

In order to impose periodicity of the RVE, the distance between two fibers of coordinates $\boldsymbol{l}$ and $\boldsymbol{m}$, is not given by the Euclidean distance, but must be calculated as (Catalanotti, 2016):

$$d_{lm} = \sqrt{\sum_{j=1}^{3}\left(min\left\{\left|\boldsymbol{l}(j)-\boldsymbol{m}(j)\right|, \boldsymbol{H}(j)-\left|\boldsymbol{l}(j)-\boldsymbol{m}(j)\right|\right\}\right)^2} \tag{12.16}$$

where $\boldsymbol{H} = \left\{H_x, H_y, H_z\right\}^T$. To calculate $\overline{\rho}_K^I$, the control point, K is iteratively moved by $\Delta\rho$ until when, after s iterations, the contact between the fiber and the

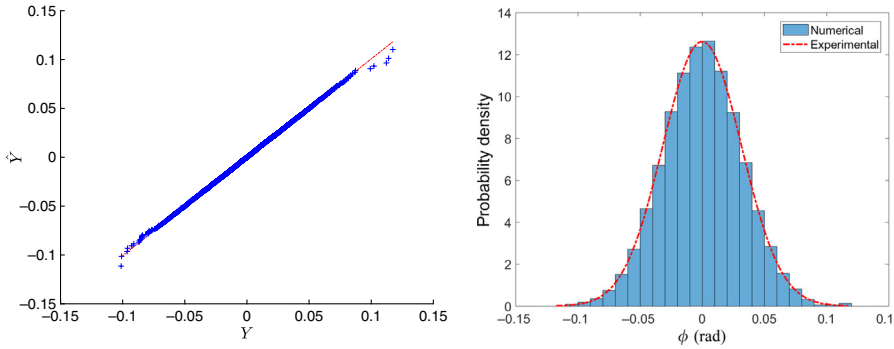

Figure 12.5 Experimental and numerical distributions obtained by minimizing the SE of the probability: (A) Q-Q plot. (B) pdf of the distributions.
Source: After Catalanotti, G., Sebaey, T., 2019. An algorithm for the generation of three-dimensional statistically representative volume elements of unidirectional fiber-reinforced plastics: focusing on the fibres waviness. Compos. Struct. 227, 111272.

surrounding ones occurs [$min(d_{lm}) < 2R$, being R the radius of the fibers]. Therefore, the maximum value of the radial coordinate, $\overline{\rho}_K^I$, is taken as $\overline{\rho}_K^I = s\Delta\rho$.

With the Bézier formulation, it is straightforward to impose periodicity in the x direction, since it is sufficient to impose C^0 and C^1 continuity between the first point of a fiber and the nth control point of its translation in the longitudinal direction. If $\boldsymbol{P}_0$ and $\boldsymbol{P}_{n-1}$ are the coordinates of the first and last control points, C^0 continuity is achieved when (end point interpolation property):

$$\boldsymbol{P}_0 = \boldsymbol{P}_{n-1} - \left(\boldsymbol{P}_{n-1} \cdot \hat{i}\right)\hat{i} \tag{12.17}$$

while C^1 continuity is ensured if (end point derivative property):

$$\{\boldsymbol{P}_1 - \boldsymbol{P}_0\} \times \{\boldsymbol{P}_{n-1} - \boldsymbol{P}_{n-2}\} = 0 \tag{12.18}$$

Therefore the first, second, penultimate, and last control points, having coordinates $\boldsymbol{P}_0$, $\boldsymbol{P}_1$, $\boldsymbol{P}_{n-2}$, and $\boldsymbol{P}_{n-1}$, respectively, cannot be moved independently, but need to satisfy both Eqs. (12.17) and (12.18).

12.2.2.4 Further considerations on the proposed methodology

Transverse orthotropy

Due to the associated manufacturing process, the UD composite material may not be a perfect transversely isotropic material, but transverse orthotropic. This means that the in-plane and out-of-plane angles (ϕ_{zx} and ϕ_{yx}, respectively) exhibit different distributions (see Sutcliffe et al., 2012), and it will be necessary to define a combined cost function. Without loss of generality, it will be possible to choose λ_I^K at the Ith iteration as:

$$\lambda_I^K = \underset{\lambda_I^K \in [0,1]}{\operatorname{argmin}} \left\{ \mathrm{SE}\left(\phi_{zx}\right) + \mathrm{SE}\left(\phi_{yx}\right) \right\} \tag{12.19}$$

which will provide two distinct distributions for ϕ_{zx} and ϕ_{yx}, as shown in Fig. 12.6.

Computational cost

Eqs. (12.11), (12.15), and (12.19) are solved numerically until a minimum error ($\mathrm{SE}_{\min} \leq \mathrm{SE}_{\min}$), or a maximum number of iterations ($I \geq I_{\max}$) has been achieved. Therefore, the computational cost of the algorithm will depend on the number of fibers, n_F, the number of control points for each fiber, n, the volume fraction, v_F, the thresholds $\mathrm{SE}_{\min}$ and $I_{\max}$, and on the entity of the misalignment introduced (e.g., a von Mises distribution on κ).

Amplitude, wavelength, and number of control points

The amplitude and wavelength of the fiber play a substantial role on the compressive response of the composite (Liu et al., 2004). These are linked to the number of control points and to the desired misalignment angle distribution. It is worth to take these parameters into account by performing some preliminary numerical calibrations (Catalanotti and Sebaey, 2019).

12.2.3 Generation of the representative volume elements in Rhino and Abaqus

Using Python (Lutz, 2003), it is possible to import the coordinates of each control point into Rhino 5 (Rhino Developer Docs, 2019), in order to generate the isolated solids of both fibers and matrix (Fig. 12.7).

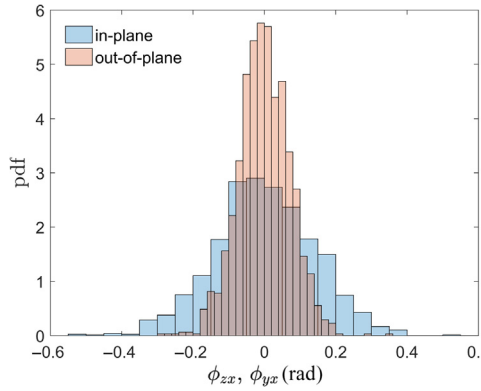

Figure 12.6 Optimized distributions for the in-plane and out-of-plane angles.
Source: After Catalanotti, G., Sebaey, T., 2019. An algorithm for the generation of three-dimensional statistically representative volume elements of unidirectional fiber-reinforced plastics: focusing on the fibres waviness. Compos. Struct. 227, 111272.

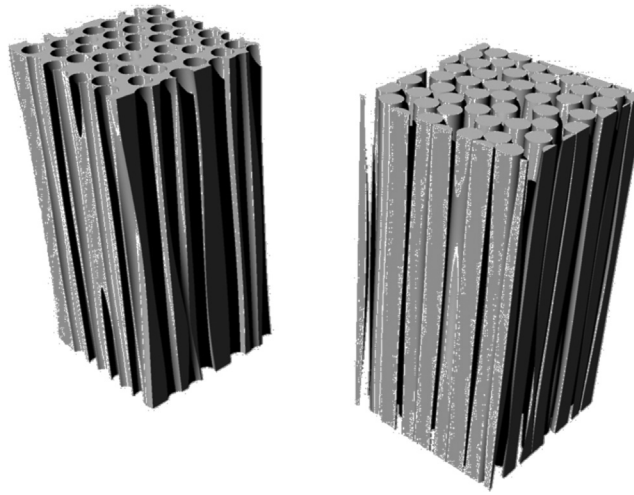

Figure 12.7 Rhino model for matrix (on the left) and fibers (on the right).

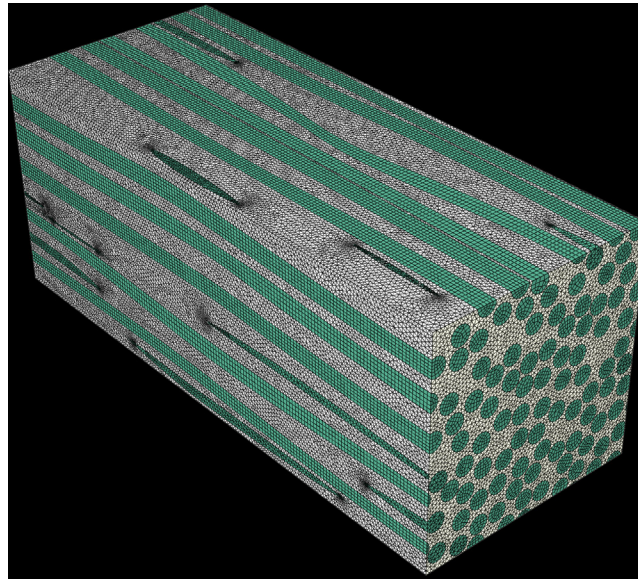

Figure 12.8 RVE generated in Abaqus CAE ($v_F = 0.5$, $n = 6$), von Mises distribution with $\kappa = 2000$.

The SAT (Standard ACIS Text format) files of both geometries are then exported from Rhino 5 and imported, by using another Python script, into Abaqus (Simulia, 2011) for the generation of the full Abaqus finite element (FE) model (see Fig. 12.8).

12.3 Constitutive models

The 3D RVEs generated contain two different constituent materials—the fiber and the matrix—and the interface between them. The following is a brief description of the constitutive models used for each of them.

12.3.1 Fiber

The fibers are considered to be transversely isotropic materials with a linear-elastic model up to failure when loaded in tension. The free energy density of the fibers is defined as:

$$\mathscr{G}_f = \frac{\sigma_{11}^2}{2E_1(1-d_f)} + \frac{\sigma_{22}^2+\sigma_{33}^2}{2E_2(1-d_f)} - \frac{\nu_{12}}{E_1}(\sigma_{11}\sigma_{22} + + \sigma_{11}\sigma_{33}) - \\ - \frac{\nu_{23}}{E_2}\sigma_{22}\sigma_{33} + \frac{\sigma_{12}^2+\sigma_{13}^2}{2G_{12}(1-d_f)} + \frac{\sigma_{23}^2}{2G_{23}(1-d_f)} \tag{12.20}$$

where E_1 and E_2 are the longitudinal and transverse Young's moduli, respectively, ν_{12} and ν_{23} are the in- and out-of-plane Poisson's ratios, respectively, G_{12} and G_{23} are the in- and out-of-plane shear moduli, respectively, and d_f is the damage variable for the fibers. Damage is activated when the following damage function is satisfied:

$$F_f = \phi_f - r_f \leq 0 \tag{12.21}$$

where r_f is the damage internal variable. The loading function ϕ_f is defined as follows:

$$\phi_f = \frac{\sim\sigma_{11}}{X_f^t} \tag{12.22}$$

where X_f^t is the longitudinal tensile strength and $\sim\sigma_{11}$ corresponds to the undamaged longitudinal stress component. The longitudinal tensile strength of the fiber follows a Weibull probability distribution (Weibull, 1951), that is, it takes into account possible defects in the material, following the equation:

$$X_f^t = \sigma_0\left[-\frac{L_0}{L}\ln(1-X)\right]^{1/m_0} \tag{12.23}$$

where σ_0 and m_0 are the Weibull strength and parameter, respectively, L_0 and L are the reference and longitudinal element length, respectively, and X is a random scalar generated in the open interval (0,1).

The following damage evolution law is defined:

$$d_f = 1 - \frac{e^{A_f(1-r_f)}}{r_f} \tag{12.24}$$

where the parameter A_f represents a mesh regularization parameter which conveys the numerical model with mesh size independency (Bažant and Oh, 1983), and is defined by the following:

$$A_f = \frac{2X_f^{t2} l^e}{2E_1 \mathscr{G}_{Ic}^f - X_f^{t2} l^e} \tag{12.25}$$

where the parameter l^e represents the characteristic element length and $\mathscr{G}_{Ic}^f$ is the critical energy release rate in mode I of the fiber.

The properties used are summarized in Table 12.1.

12.3.2 Matrix

The matrix follows a thermodynamically consistent elasto-plastic with damage constitutive behavior proposed by Melro et al. (2013a). The nonlinear plastic behavior is defined by a hydrostatic pressure−dependent yield criterion:

Table 12.1 Material properties of AS4 carbon fibers (Soden et al., 1998; Tavares et al., 2016).

Material property	Value
Fiber diameter	
$2R$ (mm)	0.007
Young's moduli	
E_{11}(MPa)	225,000
E_{22}(MPa)	15,000
Poisson's ratio	
$\nu_{12}(-)$	0.2
Shear moduli	
G_{12}(MPa)	15,000
G_{23}(MPa)	7000
Mode I fracture toughness	
$\mathscr{G}_{Ic}^f$ (N/mm)	0.01
Weibull parameters	
σ_0(MPa)	4275
$m(-)$	10.7
l_0(mm)	12.7
Density	
ρ (kg/mm^3)	1.78×10^{-6}

$$\Phi = 6J_2 + 2(\sigma_c - \sigma_t)I_1 - 2\sigma_c\sigma_t \tag{12.26}$$

where σ_t and σ_c represent the yield strengths in tension and compression, respectively, J_2 is the second invariant of the deviatoric stress tensor, and I_1 is the first invariant of the stress tensor. A non-associative flow rule, which respects the volumetric deformation of the material, is used here and it is defined by:

$$g = \sigma_{vm}^2 + \alpha p^2 \tag{12.27}$$

where σ_{vm} represents the von Mises equivalent stress, p is the hydrostatic pressure, and α is given by:

$$\alpha = \frac{9}{2}\frac{1-2\nu_p}{1+\nu_p} \tag{12.28}$$

where ν_p represents the plastic Poisson's ratio.

The hardening law is provided by two piece-wise functions from the experimental characterization of an epoxy conducted by Fiedler et al. (2001).

$$\varepsilon_e^p = \sqrt{\frac{1}{1+2\nu_p^2}\varepsilon^p{:}\varepsilon^p} \tag{12.29}$$

Damage in the matrix is defined following a thermodynamically consistent approach. The free energy density of the material is defined as:

$$\begin{aligned}\mathscr{G}_m = \frac{\sigma_{11}^2+\sigma_{22}^2+\sigma_{33}^2}{2E_m(1-d_m)} - \frac{\nu_m}{E_m}(\sigma_{11}\sigma_{22}+\sigma_{22}\sigma_{33}+\sigma_{33}\sigma_{11}) + \\ + \frac{1+\nu_m}{E_m(1-d_m)}\left(\sigma_{12}^2+\sigma_{13}^2+\sigma_{23}^2\right) + \mathscr{G}_m^p\end{aligned} \tag{12.30}$$

where E_m and ν_m are the Young's modulus and Poisson's ratio of the matrix, respectively, and d_m represents the damage variable in the matrix affecting only the Young's modulus of the material. $\mathscr{G}_m^p$ is the contribution of plastic flow to the stored energy.

The damage activation function is represented by:

$$F_m^d = \phi_m^d - r_m \leq 0 \tag{12.31}$$

where r_m is an internal variable controlled by the damage evolution law and ϕ_m^d is the loading function defined by:

$$\phi_m^d = \frac{3\tilde{J}_2}{X_m^c X_m^t} + \frac{\tilde{I}_1\left(X_m^c - X_m^t\right)}{X_m^c X_m^t} \tag{12.32}$$

where X_m^t and X_m^c represent the tensile and compressive ultimate strengths of the matrix material, respectively, and the two invariants $\tilde{J}_2$ and $\tilde{I}_1$ are determined using the concept of effective stresses defined as:

$$\sim\boldsymbol{\sigma} = \boldsymbol{H}_m^{o^{-1}} : \boldsymbol{\varepsilon} \tag{12.33}$$

where $\boldsymbol{H}_m^o$ is the undamaged compliance tensor. Bažant and Oh's (1983) crack band model is applied here in order to eliminate mesh size dependency from the constitutive formulation. The damage evolution law considered here is defined as:

$$d_m = 1 - \frac{e^{A_m\left(3-\sqrt{7+2r_m^2}\right)}}{\sqrt{7+2r_m^2}-2} \tag{12.34}$$

where the parameter A_m needs to be computed from the crack band model by equating the energy dissipated per unit volume to the ratio G_{fm}/l^e, where G_{fm} is the energy release rate of the matrix in mode I and l^e is the characteristic element length. The reader is directed to Melro et al. (2013a) for further details on the implementation of the constitutive model for the matrix.

The properties used to model the matrix constituent are summarized in Table 12.2.

Table 12.2 Matrix material properties (Fiedler et al., 2001; Arteiro et al., 2014, 2015).

Material property	Value
Young's modulus E_m(MPa)	3760
Poisson's ratio $\nu_m(-)$	0.39
Plastic Poisson's ratio $\nu_p(-)$	0.3
Tensile strength X_m^t (MPa)	93
Compressive strength X_m^c (MPa)	180
Mode I fracture toughness $\mathcal{G}_{Ic}^m$ (N/mm)	0.277
Density ρ (kg/mm^3)	1.3×10^{-6}

12.3.3 Interface

The interface between fiber and matrix follows a traditional bi-linear cohesive formulation. Given the intricate mesh required for this RVE, an Abaqus in-built cohesive surface approach was used, as it does not require mesh compatibility between the two constituents. A Mohr−Coulomb friction condition has also been considered between fiber and matrix for after failure of the cohesive bond between the two constituents. This will capture the pull-out resistance between fiber and matrix caused mostly by the rough failure surface on the fiber after cohesive interface failure.

The properties used for the cohesive model can be found in Table 12.3.

12.4 Micromechanical simulations

Analytical models are sometimes useful to understand the effect of some key parameters on the failure of UD composite materials (Camanho and Lambert, 2006; Catalanotti and Camanho, 2013). However, they are still unable to capture all damage mechanisms that occur in this type of material. Therefore, it is necessary to resort to numerical models, namely computational micromechanics, which is able to capture the individual constitutive behavior of the constituents and their interaction. In order to explore the capabilities of having a realistic microstructural construction of the composite, numerical simulations involving matrix degradation, fiber-matrix debonding, and fiber breakage are conducted by subjecting the RVEs presented in Section 12.2 to pure longitudinal tensile and compressive loading conditions. The micromechanical simulations were undertaken using the FE solver

Table 12.3 Fiber-matrix interface properties (Melro et al., 2013b; Arteiro et al., 2014, 2015).

Material property	Value
Interface stiffness	
K (N/mm^3)	10^8
Interface strengths	
τ_1^0 (MPa)	75
τ_2^0 (MPa)	75
τ_3^0 (MPa)	50
Interface fracture toughness	
$\mathcal{G}_{Ic}$ (N/mm)	0.002
$\mathcal{G}_{IIc}$ (N/mm)	0.006
$\mathcal{G}_{IIIc}$ (N/mm)	0.006
Mixed-mode interaction parameter	
η (−)	1.45
Friction coefficient	
μ_τ (−)	0.52

Abaqus/Explicit (Simulia, 2011), having the objective of analyzing the effect of fiber misalignment on the mechanical performance of the material. Fully damaged elements having $d_f > 0.9999 \vee d_m > 0.9999$ [see Eqs. (12.24) and (12.34)] were removed throughout the numerical simulations to prevent excessive element distortion. The models ran in one node (20 CPUs @ 3.4 GHz of Intel Haswell) having 512 GB of RAM. The *variable mass scaling* capability of Abaqus/Explicit was used in order to reduce computational cost, by scaling all masses of the elements, in order that they have the same time increment, that is, $\Delta_t = 1 \times 10^{-7}$ s. Quasi-static simulations were conducted by ensuring a correct energy balance throughout the simulations (Simulia, 2011).

12.4.1 Longitudinal tension

Modelling fiber-dominated failure modes of UD composite materials can be troublesome, due to the complex damage mechanisms which are inherent to these types of materials when subjected to longitudinal tension. Micromechanical computational models are appealing to study this type of failure, since the behavior of the reinforcements can be modelled independently. Fiber fracture is usually taken into account by using maximum stress criteria (Swolfs et al., 2015a,b; Tavares et al., 2017, 2019). However, for high-fidelity analysis, thermodynamically consistent damage models must be used (Tavares et al., 2016).

There are several important factors to take into consideration when modelling this type of failure, namely: (1) the stochastic nature of the longitudinal tensile strength of carbon fibers along their length, mostly due to the flaws present on the surface of the fibers (Lamon, 2007; Tanaka et al., 2014; Torres et al., 2017); (2) the formation and propagation of clusters of broken fibers (Scott et al., 2011, 2012; Thionnet et al., 2014); (3) accurately capture the full extent of the ineffective length in a broken fiber; and (4) interpret fiber failure as a dynamic process (Swolfs et al., 2015c; Tavares et al., 2019).

There are several models in the literature which can tackle most (if not all) of the aforementioned features governing longitudinal tensile failure. However, they all consider perfectly aligned fibers, not taking into account the local stress fluctuations along the reinforcing material caused by fiber waviness. For that, a similar approach modelled by Tavares et al. (2016) is presented in this section, in an attempt to evaluate the effect of fiber misalignment on the longitudinal tensile failure of UD composite materials.

12.4.1.1 Details of the finite element models

Virtual microstructures having different degrees of misalignment, that is, different von Mises distribution parameters, κ, are modelled in order to assess the effect of fiber waviness on the longitudinal tensile response. Here, RVEs having in-plane and longitudinal dimensions of approximately $29R \approx 100$ μm and $171R \approx 600$ μm, respectively, are considered. These dimensions should play a role on the mechanical response of the material, where sufficiently big dimensions are

needed in order to capture certain features which are intrinsic to longitudinal tensile failure of UD composites. However, since the correct definition of the dimensions of the FE models is not part of the scope of this chapter, the aforementioned dimensions were deemed sufficient. Due to the extremely high computational cost of these micromechanical models, only one simulation was conducted per concentration parameter, κ. All RVEs have a fiber volume fraction of $v_F = 0.55$.

Regarding the applied boundary conditions, since periodic boundary conditions (PBCs) are computationally very expensive, and by considering a sufficiently big RVE, a simplified version of these was used by constraining the displacements of the opposite faces in the RVE using Abaqus *Tie Constraints* ("Face 3" with "Face 4" and "Face 5" with "Face 6" presented in Fig. 12.9). A velocity type BC is applied in "Face 2," and the longitudinal (x-direction) axial displacement is blocked in "Face 1."

Fibers are modelled with C3D8R, reduced integration hexahedrons. Due to the complexity of the matrix part, C3D4, linear tetrahedrons are used to model it. The FE models have an average seed size of 1.2 μm, with 200 elements along their length, equating to a total number of elements of $\approx 7,000,000$ ($\approx 1,200,000$ elements for the fibers and $\approx 5,800,000$ elements for the matrix).

12.4.1.2 Numerical results

The longitudinal tensile stress−strain curves of four different types of RVEs having $\kappa = 2000$, $\kappa = 4000$, $\kappa = 8000$, and $\kappa = \infty$ are shown in Fig. 12.10.

It can be seen that the overall longitudinal tensile mechanical response of the material is not substantially affected by the initial fiber misalignment. Even if the Young's modulus slightly decreases with increasing misalignment, the peak stresses are all very similar. The same cluster-type formation was observed for all RVEs, despite their misalignment. The majority of fibers did not fail in the same plane, leading to the formation of disperse clusters, where the locations of fiber breaks are

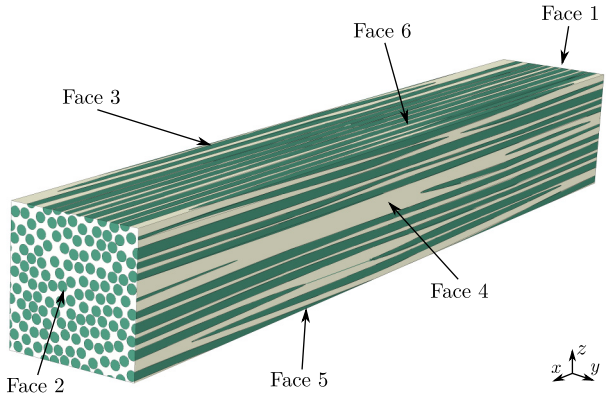

Figure 12.9 Representation of a high-fidelity micromechanical RVE, highlighting its different faces.

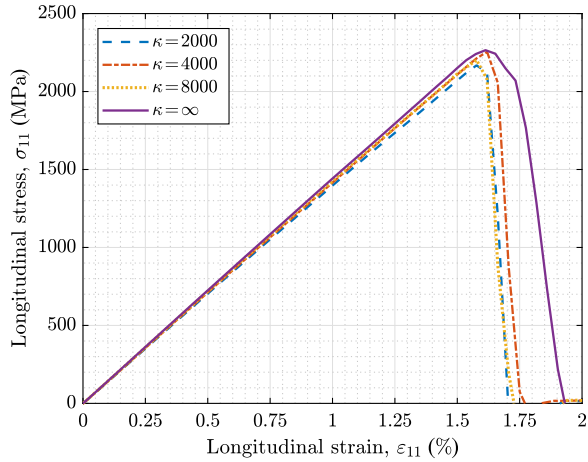

Figure 12.10 Longitudinal tensile stress−strain curves of four RVEs having different distributions of initial misalignments, κ.

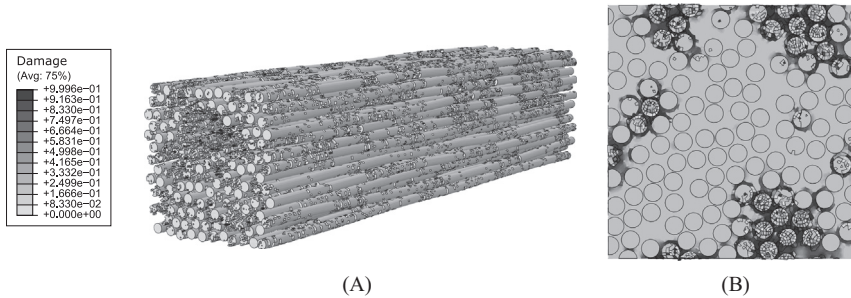

Figure 12.11 Contour plots of both matrix and fibers damage variable for: (A) an RVE having $\kappa = 4000$, just after peak load, highlighting the different damage events occurring in a disperse manner; (B) an RVE having $\kappa = 2000$, before peak load, highlighting the formation of coplanar clusters.

observed in multiple locations (see Fig. 12.11A). However, as it can be seen from Fig. 12.11B, in some cases, the clustering process was also coplanar.

Performing a more local analysis, Fig. 12.12 shows the contour plots of the longitudinal stress (S11), and fiber-matrix interface damage (CSDMG), highlighting the ineffective and debond lengths of two different fibers, namely: (A) a perfectly straight fiber embedded in an RVE having perfectly aligned and parallel fibers and (B) a misaligned fiber embedded in an RVE having $\kappa = 4000$.

From the qualitative results here presented, it seems that, for these two fibers, the ineffective length slightly increases when increasing fiber misalignment, possibly leading to a faster progression of a bigger cluster and causing the material to fail earlier. Moreover, it was noted that the breakage of the higher misaligned fibers

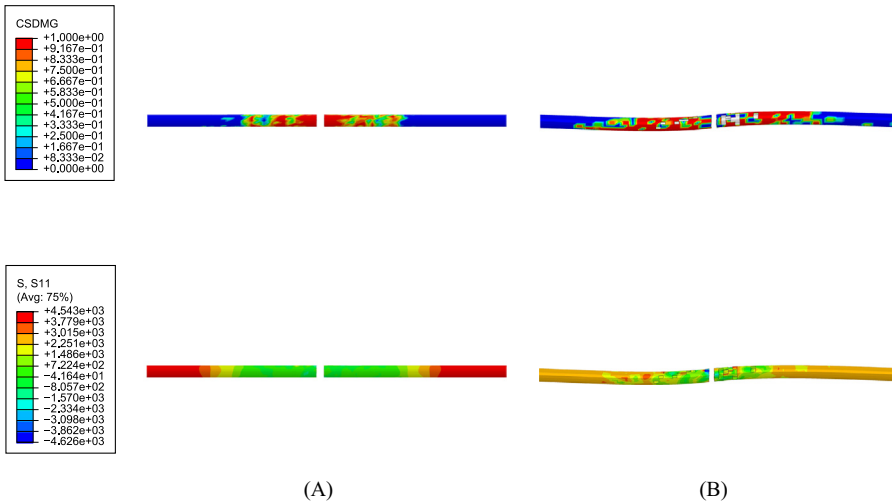

Figure 12.12 Contour plots of the longitudinal stress (S11) and fiber-matrix interface damage (CSDMG) of an aligned and a misaligned fiber.

occurred at lower applied displacements, possibly leading to a faster stress redistribution to the neighboring fibers. However, from the aforementioned quantitative results (see Fig. 12.10), it can be concluded that the final failure of the material is not directly connected to the effects acting in a single fiber, but of a bigger collection of fibers, therefore possibly making these damage mechanisms, which act in a particular region of a single fiber, be neglected comparing to the presence of flaws, which is here taken into account through the variation in the longitudinal tensile strength through a Weibull distribution.

12.4.2 Longitudinal compression

Fiber kinking represents the primary failure mechanism when a UD laminate is loaded under longitudinal compression (Kyriakides et al., 1995; Moran et al., 1995; Budiansky et al., 1998) (see Fig. 12.13). There is compelling evidence that this mode of failure is mostly controlled by the initial fiber misalignment and the shear yield strength of the matrix (Moran et al.,1995; Vogler and Kyriakides, 1999; Bažant et al., 1999; Gutkin et al., 2010). During compressive loading, the first appearance of nonlinearity is due to the plastic nature of the epoxy, causing the fibers to rotate [also known as "incipient kinking" (Moran et al., 1995)]. Due to this rotation and to the formation of microcracks in the resin, the peak load is reached, forming an initial kink-band. The progressive shearing/bending causes the continuous degradation of the material, until this fiber rotation is halted, causing the blocking of the fibers (fiber lock-up). This locking leads to the broadening of the kink-band, causing a constant stress plateau under compression, referred as the residual

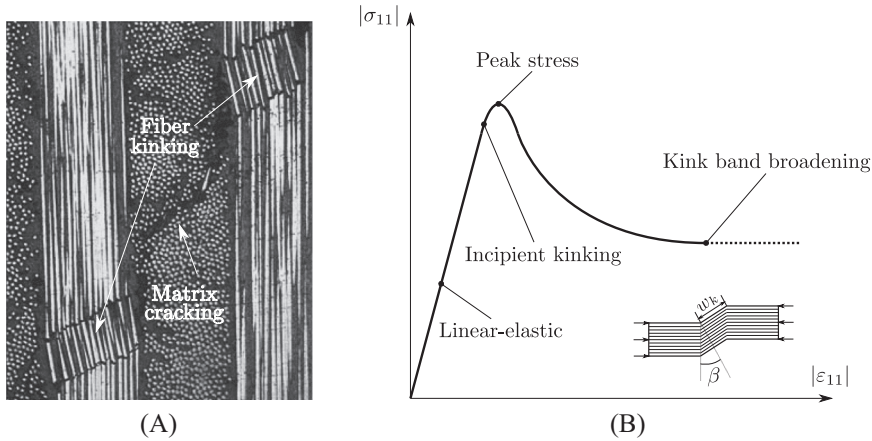

Figure 12.13 (A) Micrographs of the kink-band formed in a UD cross-ply laminate; (B) schematic representation of the longitudinal compressive behavior of a UD composite material, highlighting the different load level stages.
Source:(A) adapted from Pinho, S.T., Robinson, P., Iannucci, L., 2006. Fracture toughness of the tensile and compressive fiber failure modes in laminated composites, Compos. Sci. Technol. 66 (13), 2069−2079. (B) adapted from Moran, P.M., Liu, X.H., Shih, C.F., 1995. Kink-band formation and band broadening in fiber composites under compressive loading. Acta Metallurgica et. Materialia 43 (8), 2943−2958.

compressive strength of the material (Dalli et al., 2020; Moran et al., 1995; Zobeiry et al., 2015).

The mesomechanical compressive longitudinal behavior of UD composite materials has been extensively modelled in the past by several authors (e.g., Maimí et al., 2007; Van Der Meer and Sluys, 2009; Tan et al., 2015, 2016; Gutkin et al., 2016; Larsson et al., 2018). However, being compressive failure essentially dominated by low-scale failure mechanisms, micromechanical computational models revealed to be ideal tools to capture the high level of detail which are intrinsic to such materials (Camanho and Arteiro, 2017; Arteiro et al., 2018). Even if simple 2D and 3D micromechanical models were developed in the past to evaluate (Hsu et al., 1998, 1999; Yerramalli and Waas, 2004; Bai et al., 2015; Naya et al., 2017; Herraez et al., 2018), instead of using an empirical distribution for the fiber waviness (Catalanotti and Sebaey, 2019; Sebaey et al., 2019), consequently creating an unrealistic kink region in a narrow band at the central part of the model, causing erroneous numerical predictions and constant kink-band angles and widths. Moreover, some studies used volumetric computational averaging techniques to homogenize the stress during loading (Naya et al., 2017; Herraez et al., 2018), and compared the results with experimental observations. However, it is not clear if this is an appropriate measure of the actual longitudinal strength of the material, as the material response during softening is known to depend on both boundary conditions and size of the RVE (Gitman et al., 2007).

This section aims to briefly address the fiber kinking phenomenon using an accurate representation of the microstructural behavior of the composite, and appropriate constitutive material models for the constituents and their interface, which are described in Section 12.3.

12.4.2.1 Details of the finite element models

Different RVEs are generated in order to assess the influence of the distribution of the initial fiber misalignment on the longitudinal compressive behavior. For that, the generated RVEs have the same fiber volume fraction ($v_F = 0.55$) and different concentration parameters, κ (see Section 12.2 for reference) from 1000 (very wavy fibers) to ∞ (perfectly aligned fibers). According to experimental observations (Sebaey et al., 2019), for two different thermoset and thermoplastic carbon fiber composites, this value lied within the range $1500 < \kappa < 2000$. Per concentration parameter, κ, three RVEs having distinct fiber distributions are generated to assess microstructural randomness.

As previously said, the applied boundary conditions on the RVE should influence the assessment of the mechanical performance of the microstructure, existing an interplay between the boundary conditions and the size of the RVE (Gitman et al., 2007; Galli et al., 2008). It is assumed a long enough RVE size to model longitudinal compression ($17.2R \times 17.2R \times 85R$, approximately equating to $60 \times 60 \times 300\ \mu m^3$).The displacements of faces 3 and 4 are constrained using *Tie Constraints*, faces 5 and 6 are free to deform (Hsu et al., 1998; Bishara et al., 2017), the longitudinal (x-direction) axial displacements of face 1 are blocked, as well as the through-thickness (z-direction) axial displacements, and finally, the longitudinal compressive velocity-type BC is applied in face 2 (see Fig. 12.9 for reference).

The fibrous reinforcements are modelled using C3D8R, reduced integration hexahedral solid elements, while the matrix material, since it represents a complex geometrical part (see Figs. 12.8 or 12.9), is modelled with C3D4, tetrahedral solid elements. Both are modelled with elements having an average size of 0.7 μm, having 250 elements along the length of the RVE, equating approximately to a total of 3.400, 000 elements ($\approx 900,000$ elements for the fibers and $\approx 2,400,000$ elements for the matrix).

12.4.2.2 Numerical results

Fig. 12.14 and Table 12.4 show the quantitative numerical predictions of the RVEs having different distributions of the initial fiber misalignment angle, κ. The micromechanical models are able to capture the initial linear-elastic behavior, the onset of nonlinearity caused by matrix plasticity/degradation, and collapse of the material caused by fiber kinking.

The normalized stress−strain curves (see Fig. 12.14A, where σ_{11} and ε_{11} represent the undergoing longitudinal stress and engineering strain, respectively, and $\sigma^u_{11_\infty}$ and $\varepsilon^u_{11_\infty}$ represent the peak stress and corresponding engineering strain of the

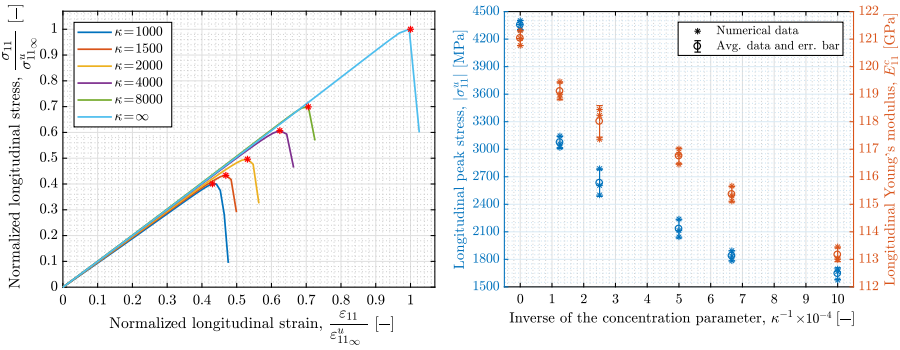

Figure 12.14 Effect of fiber misalignment on the longitudinal compressive behavior: (A) normalized representative compressive stress−strain curves (the highlighted red points indicate the ultimate stress); (B) sensitivity results for compressive peak stress and Young's modulus, where both individual numerical results, and corresponding mean and standard deviation values are shown.

Table 12.4 Numerical predictions of the mean compressive Young's modulus, E^c_{11}, and peak stresses, σ^u_{11}, and corresponding standard deviations, for different von Mises concentration parameters, κ.

	$\kappa = 1000$	$\kappa = 1500$	$\kappa = 2000$	$\kappa = 4000$	$\kappa = 8000$	$\kappa = \infty$
E^c_{11} (GPa)	$113.2^{\pm 0.3}$	$115.4^{\pm 0.3}$	$116.8^{\pm 0.3}$	$118.0^{\pm 0.6}$	$119.1^{\pm 0.3}$	$121.0^{\pm 0.3}$
σ^u_{11} (MPa)	$1645^{\pm 50}$	$1837^{\pm 65}$	$2132^{\pm 145}$	$2632^{\pm 99}$	$3074^{\pm 55}$	$4354^{\pm 63}$

RVE having $\kappa = \infty$) show that both compressive Young's modulus, E^c_{11} and peak stress, σ^u_{11} depend on κ. As κ increases (less misalignment), the mechanical performance of the material increases as well, where the RVEs having the highest misalignment ($\kappa = 1000\$$) showed to yield a peak stress of $\approx 40\%$ of the idealized RVE having perfectly aligned fibers ($\kappa = \infty$). The decrease on the peak stress is justified by the initial micro-buckling introduced to the fibers, causing an earlier degradation of the matrix and fiber-matrix interface, promoting earlier fiber kinking. Comparing the results with experimental values of the compressive strength of different composite materials, namely with AS4/8552 ($X^C \approx 1530$ MPa), IM7/8552 ($X^C \approx 1689$ MPa), and IM10/8552 ($X^C \approx 1793$ MPa) (Hexcel, 2016), it is evident that only the RVEs which have a more realistic initial fiber misalignment angle distribution ($\kappa \leq 1500$) yielded peak stresses comparable to the empirical compressive strength of these materials.

The kink-band width, w_k, was qualitatively obtained as the distance between the two extreme points of the kink-band which have the hightest longitudinal stress (Pimenta et al., 2009). Even if it is probably needed thicker RVEs to properly

characterize the kink-band angle, β (Herraez et al., 2018), here, it was obtained by measuring the angle of the kink-band with a vertical line (see Fig. 12.13). All RVEs exhibited similar kink-band widths ($w_k^{\text{avg}} \approx 85\ \mu$m) and angles ($\beta^{\text{avg}} \approx 12^{\circ}$). Fig. 12.15 shows the contour plots of the equivalent plastic strain of three different deformed RVEs having different initial fiber misalignment distributions, just before instability, highlighting the kink-band widths and angles. It can be seen that, due to the realistic representation of the micromechanical geometry, the kink-band does not necessarily occur in the center of the RVE, since the 3D spatial distribution of the reinforcements is random. According to previous experimental results, the kink-

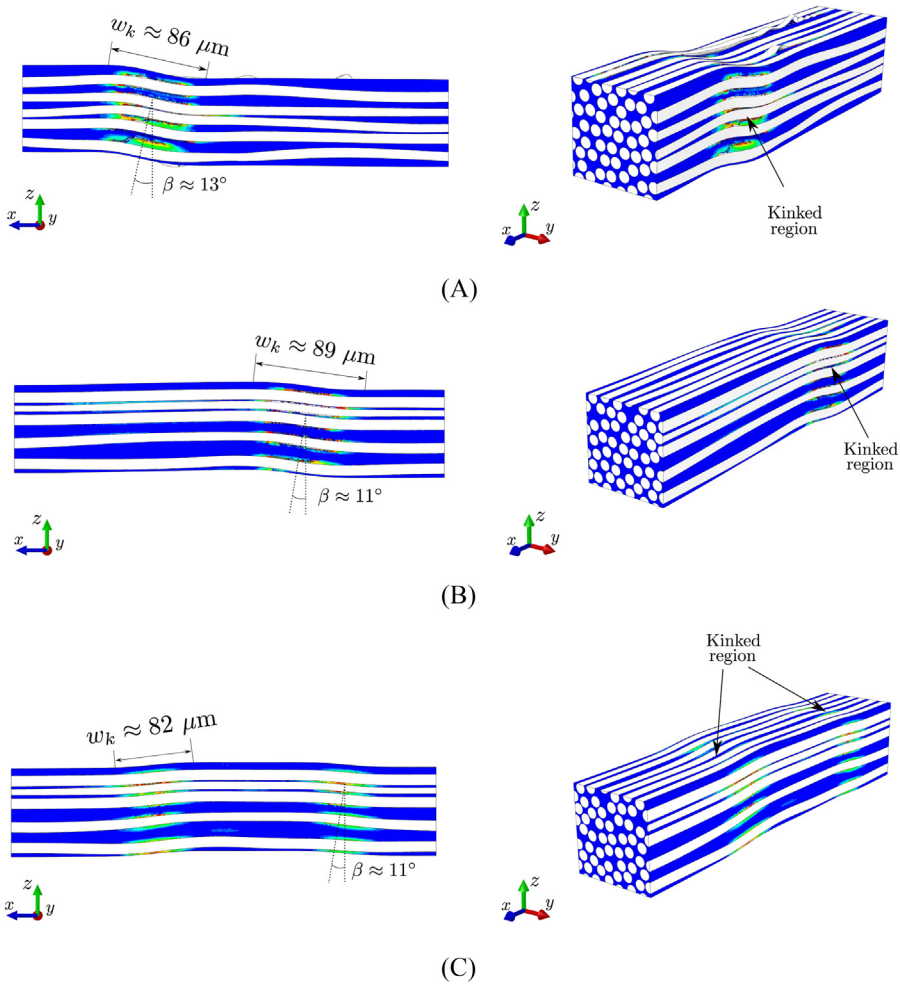

Figure 12.15 Contour plots of the equivalent plastic strain of the epoxy matrix (red = 0.22; yellow = 0.11; and blue = 0) for RVEs having: (A) $\kappa = 1500$; (B) $\kappa = 2000$; and (C) $\kappa = 4000$.

band width and angle have reported to be $50\ \text{mm} \leq w_k^{exp} \leq 100\ \text{mm}$ (Pinho et al., 2006; Jumahat et al., 2010; Hapke et al., 2011; Zobeiry et al., 2015) and $10^\circ \leq \beta^{exp} \leq 25^\circ$ (Fleck and Jelf, 1995; Moran et al., 1995; Vogler and Kyriakides, 2001; Bergan and Garcea, 2017), for different thermoset-based composite materials, thus concluding that the micromechanical models are able to take into account both features of the longitudinal compressive failure.

12.5 Conclusions

The information presented in this chapter represents the first step toward high-fidelity micromechanical modelling of UD composite materials, where the 3D geometric variability of the material is taking into account. Making use of the appropriate constitutive material models for the constituents and their interface, numerical analyses were undertaken in order to evaluate the effect of the initial fiber waviness on the longitudinal failure of such materials. The main findings of this work can be summarized as follows:

- A numerical algorithm was presented that generates the angle misalignment distribution of the fibrous reinforcements, combining a stochastic process with an optimization procedure, in order to obtain a higher degree of similarity between the experimental and numerical distributions. The fibers were modelled as Bézier curves, whose control points can be moved in a random fashion in order to introduce the desired misalignment, allowing an easy implementation of PBCs on the RVEs. Moreover, due to their precise analytical description, their geometry can be simply described and exported making sole use of the coordinates of the fibers control points.
- The numerical results presented here show that fiber misalignment has a small effect on the overall longitudinal tensile performance of the material (see Fig. 12.10). All RVEs presented relatively the same failure mechanisms, where cluster development occurred in both disperse and coplanar manners (see Fig. 12.11). However, analyzing the fiber failure locations, it can be seen that the ineffective length of the fibers may increase with increasing fiber misalignment (see Fig. 12.12), possibly leading to a faster stress redistribution. However, it is not certain if these smaller scale mechanisms play a decisive role on the overall longitudinal tensile failure.
- The aforementioned results show that there is an intrinsic dependency of the fiber misalignment on the longitudinal compressive failure of such materials. A clear decrease on the compressive mechanical performance (Young's modulus and ultimate load) can be evidenced when increasing fiber misalignment (see Fig. 12.14 and Table 12.4). Qualitatively, the micromechanical models exhibited values of kink-band widths and kink angles which were consistent with experimental observations (see Fig. 12.15).

With the results presented here, it can be concluded that once again, computational micromechanics can be treated as a reliable tool to evaluate the performance of heterogeneous materials. However, despite the advances that took place, these results represent only a part of the outputs which can be extracted using micromechanics. Therefore, several other analyses need to be conducted, such as: (1) evaluate the effect of fiber-matrix interface properties; (2) model bigger RVEs (namely

in the in-plane directions) to enable a more detailed inspection of certain damage mechanisms; (3) analyze the evolution of fiber rotation with compressive loading; (4) evaluate the kink-band broadening phenomenon; and (5) evaluate the role of fiber nonlinearity under compression. A subsequent study conducted by the authors (Varandas et al., 2020), involved a more detailed and robust study of both longitudinal compressive and tensile behavior of CFRPs. Nevertheless, the results presented here are able to validate the realistic geometrical micromechanic representation of UD composite materials (Catalanotti and Sebaey, 2019) under longitudinal loading.

Acknowledgments

The authors gratefully acknowledge the financial support of the project ICONIC—Improving the crashworthiness of composite transportation structures. ICONIC has received funding from the European Union's Horizon 2020 research and innovation program under the Marie Sklodowska-Curie grant agreement No 721256. The content reflects only the author's view and the agency is not responsible for any use that may be made of the information it contains.

References

Altendorf, H., Jeulin, D., 2011. Random-walk-based stochastic modeling of three-dimensional fiber systems. Phys. Rev. E83, 041804.

Arteiro, A., Catalanotti, G., Melro, A.R., Linde, P., Camanho, P.P., 2014. Micro-mechanical analysis of the in situ effect in polymer composite laminates. Compos. Struct. 116 (1), 827−840.

Arteiro, A., Catalanotti, G., Melro, A.R., Linde, P., Camanho, P.P., 2015. Micro-mechanical analysis of the effect of ply thickness on the transverse compressive strength of polymer composites. Compos. A Appl. Sci. Manuf. 79, 127−137.

Arteiro, A., Catalanotti, G., Reinoso, J., Linde, P., Camanho, P.P., 2018. Simulation of the mechanical response of thin-ply composites: From computational micro-mechanics to structural analysis. Arch. Comput. Methods Eng. 26, 1445−1487.

Bai, X., Bessa, M.A., Melro, A.R., Camanho, P.P., Guo, L., Liu, W.K., 2015. High-fidelity micro-scale modeling of the thermo-visco-plastic behavior of carbon fiber polymer matrix composites. Compos. Struct. 134, 132−141.

Bažant, Z.P., Kim, J.-J. H., Daniel, I.M., Becq-Giraudon, E., Zi, G., 1999. Size effect on compression strength of fiber composites failing by kink band propagation. Int. J. Fract. 95103.

Bažant, Z.P., Oh, B.H., 1983. Crack band theory for fracture of concrete. Mater. Struct. 16 (3), 155−177.

Bergan, A.C., Garcea, S.C., 2017. In-situ observations of longitudinal compression damage in carbon-epoxy cross-ply laminates using fast synchrotron radiation computed tomography. In: 32nd American Society for Composites Technical Conference, West Lafayette, IN.

Bishara, M., Rolfes, R., Allix, O., 2017. Revealing complex aspects of compressive failure of polymer composites—Part I: fiber kinking at microscale. Compos. Struct. 169, 105–115.

Budiansky, B., Fleck, N.A., Amazigo, J.C., 1998. On kink-band propagation in fiber composites. J. Mech. Phys. Solids 46, 1637–1653.

Camanho, P.P., Arteiro, A., Melro, A.R., Catalanotti, G., Vogler, M., 2015. Three-dimensional invariant-based failure criteria for fibre-reinforced composites. Int. J. Solids Struct. 55, 92–107. Special Issue Computational and Experimental Mechanics of Advanced Materials A workshop held at King Abdullah University of Science and Technology Jeddah, Kingdom of Saudi Arabia July 1-3, 2013.

Camanho, P.P., Lambert, M., 2006. A design methodology for mechanically fastened joints in laminated composite materials. Compos. Sci. Technol. 66 (15), 3004–3020.

Camanho, P.P., Arteiro, A., 2017. Analysis models for polymer composites across different length scales. The Structural Integrity of Carbon Fiber Composites. Springer International Publishing, pp. 199–279.

Catalanotti, G., 2016. On the generation of RVE-based models of composites reinforced with long fibres or spherical particles. Compos. Struct. 138, 84–95.

Catalanotti, G., Camanho, P.P., 2013. A semi-analytical method to predict net-tension failure of mechanically fastened joints in composite laminates. Compos. Sci. Technol. 76, 69–76.

Catalanotti, G., Sebaey, T.A., 2019. An algorithm for the generation of three-dimensional statistically representative volume elements of unidirectional fibre-reinforced plastics: focusing on the fibres waviness. Compos. Struct. 227, 111272.

Clarke, A.C., Archenhold, G., Davidson, N.C., 1995. A novel technique for determining the 3D spatial distribution of glass fibres in polymer composites. Compos. Sci. Technol. 55 (1), 75–91.

Creighton, C.J., Sutcliffe, M.P.F., Clyne, T.W., 2001. A multiple field image analysis procedure for characterisation of fibre alignment in composites. Compos. A Appl. Sci. Manuf. 32 (2), 221–229.

Dalli, D., Catalanotti, G., Varandas, L.F., Falzon, B.G., Foster, S., 2020. Compressive intralaminar fracture toughness and residual strength of 2D woven carbon fibre reinforced composites: New developments on using the size effect method. Theoretical and Applied Fracture Mechanics 106102487.

Faessel, M., Delise, C., Bos, F., Castra, P., 2005. 3D modelling of random cellulosic fibrous networks based on X-ray tomography and image analysis. Compos. Sci. Technol. 65 (13), 1931–1940.

Fiedler, B., Hojo, M., Ochiai, S., Schulte, K., Ando, M., 2001. Failure behavior of an epoxy matrix under different kinds of static loading. Compos. Sci. Technol. 61 (11), 1615–1624.

Fleck, N.A., Jelf, P.M., 1995. Deformation and failure of a carbon fibre composite under combined shear and transverse loading. Acta Metallurgica et. Materialia 43 (8), 3001–3007.

Galli, M., Botsis, J., Janczak-Rusch, J., 2008. An elastoplastic three-dimensional homogenization model for particle reinforced composites. Comput. Mater. Sci. 41 (3), 312–321.

Gitman, I.M., Askes, H., Sluys, L.J., 2007. Representative volume: existence and size determination. Eng. Fract. Mech. 74 (16), 2518–2534.

Gutkin, R., Costa, S., Olsson, R., 2016. A physically based model for kink-band growth and longitudinal crushing of composites under 3D stress states accounting for friction. Compos. Sci. Technol. 135, 39–45.

Gutkin, R., Pinho, S.T., Robinson, P., Curtis, P.T., 2010. On the transition from shear-driven fibre compressive failure to fibre kinking in notched CFRP laminates under longitudinal compression. Compos. Sci. Technol. 70 (8), 1223–1231.

Hapke, J., Gehrig, F., Huber, N., Schulte, K., Lilleodden, E.T., 2011. Compressive failure of UD-CFRP containing void defects: in situ SEM microanalysis. Compos. Sci. Technol. 71 (9), 1242–1249.

Herasati, S., Zhang, L., 2014. A new method for characterizing and modeling the waviness and alignment of carbon nanotubes in composites. Compos. Sci. Technol. 100, 136–142.

Herraez, M., Bergan, A.C., González, C., 2018. Modeling fiber kinking at the microscale and mesoscale, Technical Report, NASA/TP-2018-220105 (October).

Hexcel, 2016.HexPly® 8552 Matrix, Epoxy matrix (180°C/356°F curing matrix).

Hsu, S.-Y., Vogler, T.J., Kyriakides, S., 1998. Compressive strength predictions for fiber composites. J. Appl. Mech. 65 (1), 7–16.

Hsu, S.Y., Vogler, T.J., Kyriakides, S., 1999. On the axial propagation of kink bands in fiber composites: Part II analysis. Int. J. Solids Struct. 36 (4), 575–595.

Jumahat, A., Soutis, C., Jones, F.R., Hodzic, A., 2010. Fracture mechanisms and failure analysis of carbon fibre/toughened epoxy composites subjected to compressive loading. Compos. Struct. 92 (2), 295–305.

Kratmann, K.K., Sutcliffe, M.P.F., Lilleheden, L.T., Pyrz, R., Thomsen, O.T., 2009. A novel image analysis procedure for measuring fibre misalignment in unidirectional fibre composites. Compos. Sci. Technol. 69 (2), 228–238.

Kyriakides, S., Arseculeratne, R., Perry, E.J., Liechti, K.M., 1995. On the compressive failure of fiber reinforced composites. Int. J. Solids Struct. 32 (6-7), 689–738.

Lamon, J., 2007. Mécanique de la rupture fragile et de l'endommagement: Approches statistiques et probabilistes, hermes-lav edn Hermès Science Publications, Paris.

Larsson, R., Gutkin, R., Rouhi, M.S., 2018. Damage growth and strain localization in compressive loaded fiber reinforced composites. Mech. Mater. 127 (September), 77–90.

Liu, D., Fleck, N.A., Sutcliffe, M.P.F., 2004. Compressive strength of fibre composites with random fibre waviness. J. Mech. Phys. Solids 52 (7), 1481–1505.

Lutz, M., 2003. Learning Python, second edn O'Reilly & Associates, Inc., Sebastopol, CA.

Maimí, P., Camanho, P.P., Mayugo, J.A., Dávila, C.G., 2007. A continuum damage model for composite laminates: Part I Constitutive model. Mech. Mater. 39 (10), 897–908.

Mardia, K.V., Jupp, P.E., 2008. Directional Statistics. John Wiley & Sons, Inc.

Melro, A.R., Camanho, P.P., Andrade Pires, F.M., Pinho, S.T., 2013a. Micromechanical analysis of polymer composites reinforced by unidirectional fibres: Part I – Constitutive modelling. Int. J. Solids Struct. 50 (11–12), 1897–1905.

Melro, A.R., Camanho, P.P., Andrade Pires, F.M., Pinho, S.T., 2013b. Micromechanical analysis of polymer composites reinforced by unidirectional fibres: Part II – Micromechanical analyses. Int. J. Solids Struct. 50 (11–12), 1906–1915.

Melro, A.R., Camanho, P.P., Pinho, S.T., 2008. Generation of random distribution of fibres in long-fibre reinforced composites. Compos. Sci. Technol. 68, 2092–2102.

Moran, P.M., Liu, X.H., Shih, C.F., 1995. Kink band formation and band broadening in fiber composites under compressive loading. Acta Metallurgica et. Materialia 43 (8), 2943–2958.

Naya, F., Herráez, M., Lopes, C.S., González, C., Van der Veen, S., Pons, F., 2017. Computational micromechanics of fiber kinking in unidirectional FRP under different environmental conditions. Compos. Sci. Technol. 144, 26–35.

Pimenta, S., Gutkin, R., Pinho, S.T., Robinson, P., 2009. A micromechanical model for kink-band formation: Part II—Analytical modelling. Composites Science and Technology 69, 956−964.

Pinho, S.T., Robinson, P., Iannucci, L., 2006. Fracture toughness of the tensile and compressive fibre failure modes in laminated composites. Compos. Sci. Technol. 66 (13), 2069−2079.

Recchia, S., Zheng, J., Pelegri, A.A., 2014. Fiberwalk: a random walk approach to fiber representative volume element creation. Acta Mech. 225 (4), 1301−1312.

Requena, G., Fiedler, G., Seiser, B., Degischer, P., Michiel, M.D., Buslaps, T., 2009. 3D-quantification of the distribution of continuous fibres in unidirectionally reinforced composites. Compos. A Appl. Sci. Manuf. 40 (2), 152−163.

Rhino Developer Docs, 2019. <https://developer.rhino3d.com/guides/>.

Scott, A.E., Mavrogordato, M., Wright, P., Sinclair, I., Spearing, S.M., 2011. In situ fibre fracture measurement in carbonepoxy laminates using high resolution computed tomography. Compos. Sci. Technol. 71 (12), 1471−1477.

Scott, A.E., Sinclair, I., Spearing, S.M., Thionnet, A., Bunsell, A.R., 2012. Damage accumulation in a carbon/epoxy composite: comparison between a multiscale model and computed tomography experimental results. Compos. A Appl. Sci. Manuf. 43 (9), 1514−1522.

Sebaey, T.A., Catalanotti, G., Dowd, N.P.O., 2019. A microscale integrated approach to measure and model fibre misalignment in fibre-reinforced composites. Compos. Sci. Technol. 183 (June), 107793. Available from: https://doi.org/10.1016/j.compscitech.2019.107793.

Simulia, 2011. ABAQUS Documentation. Dassault Systèmes, Providence, RI.

Soden, P.D., Hinton, M.J., Kaddour, A.S., 1998. Lamina properties, lay-up configurations and loading conditions for a range of fibre-reinforced composite laminates. Compos. Sci. Technol. 58 (7), 1011−1022.

Stein, I.Y., Lewis, D.J., Wardle, B.L., 2015. Aligned carbon nanotube array stiffness from stochastic three-dimensional morphology. Nanoscale 7, 19426−19431.

Sutcliffe, M.P.F., Lemanski, S.L., Scott, A.E., 2012. Measurement of fibre waviness in industrial composite components. Compos. Sci. Technol. 72 (16), 2016−2023.

Swolfs, Y., McMeeking, R.M., Verpoest, I., Gorbatikh, L., 2015a. Matrix cracks around fibre breaks and their effect on stress redistribution and failure development in unidirectional composites. Compos. Sci. Technol. 108, 16−22.

Swolfs, Y., McMeeking, R.M., Verpoest, I., Gorbatikh, L., 2015b. The effect of fibre dispersion on initial failure strain and cluster development in unidirectional carbon/glass hybrid composites. Compos. A Appl. Sci. Manuf. 69, 279−287.

Swolfs, Y., Morton, H., Scott, A.E., Gorbatikh, L., Reed, P.A.S., Sinclair, I., et al., 2015. Synchrotron radiation computed tomography for experimental validation of a tensile strength model for unidirectional fibre-reinforced composites. Compos. A Appl. Sci. Manuf. 77, 106−113.

Tan, W., Falzon, B.G., Price, M., 2015. Predicting the crushing behaviour of composite material using high-fidelity finite element modelling. Int. J. Crashworthiness 20 (1), 60−77.

Tan, W., Falzon, B.G., Price, M., Liu, H., 2016. The role of material characterisation in the crush modelling of thermoplastic composite structures. Compos. Struct. 153, 914−927.

Tanaka, F., Okabe, T., Okuda, H., Kinloch, I.A., Young, R.J., 2014. Factors controlling the strength of carbon fibres in tension. Compos. A Appl. Sci. Manuf. 57, 88−94.

Tavares, R.P., Melro, A.R., Bessa, M.A., Turon, A., Liu, W.K., Camanho, P.P., 2016. Mechanics of hybrid polymer composites: analytical and computational study. Comput. Mech. 57 (3), 405−421.

Tavares, R.P., Otero, F., Baiges, J., Turon, A., Camanho, P.P., 2019. A dynamic spring element model for the prediction of longitudinal failure of polymer composites. Comput. Mater. Sci. 160 (January), 42−52.

Tavares, R.P., Otero, F., Turon, A., Camanho, P.P., 2017. Effective simulation of the mechanics of longitudinal tensile failure of unidirectional polymer composites. Int. J. Fract. 208 (1), 269−285.

Thionnet, A., Chou, H.Y., Bunsell, A., 2014. Fibre break processes in unidirectional composites. Compos. A Appl. Sci. Manuf. 65, 148−160.

Torres, J.P., Vandi, L.J., Veidt, M., Heitzmann, M.T., 2017. The mechanical properties of natural fibre composite laminates: a statistical study. Compos. A Appl. Sci. Manuf. 98 (March), 99−104.

Van Der Meer, F.P., Sluys, L.J., 2009. Continuum models for the analysis of progressive failure in composite laminates. J. Compos. Mater. 43 (20), 2131−2156.

Varandas, L.F., Catalanotti, G., Melro, A.R., Tavares, R.P., Falzon, B.G., 2020. Micromechanical modelling of the longitudinal compressive and tensile failure of unidirectional composites: The effect of fibre misalignment introduced via a stochastic process. Int. J. Solids Struct. 203, 157−176.

Vaughan, T.J., McCarthy, C.T., 2011. Micromechanical modelling of the transverse damage behaviour in fibre reinforced composites. Compos. Sci. Technol. 71, 388−396.

Vogler, T.J., Kyriakides, S., 1999. On the axial propagation of kink bands in fiber composites: Part I experiments. Int. J. Solids Struct. 36, 557−574.

Vogler, T.J., Kyriakides, S., 2001. On the initiation and growth of kink bands in fiber composites: Part I. experiments. Int. J. Solids Struct. 38 (15), 2639−2651.

Weibull, W., 1951. A statistical distribution function of wide applicability. J. Appl. Mech. 103, 293−297.

Yerramalli, C.S., Waas, A.M., 2004. The effect of fiber diameter on the compressive strength of composites − a 3D finite element based study. CMES − Comput. Model. Eng. Sci. 6 (1), 1−16.

Yurgartis, S.W., 1987. Measurement of small angle fiber misalignments in continuous fiber composites. Compos. Sci. Technol. 30 (4), 279−293.

Zobeiry, N., Vaziri, R., Poursartip, A., 2015. Characterization of strain-softening behavior and failure mechanisms of composites under tension and compression. Compos. A Appl. Sci. Manuf. 68, 29−41.